Journal of Power Sources 210 (2012) 67–80

Contents lists available at SciVerse ScienceDirect

Journal of Power Sources

journal homepage: www.elsevier.com/locate/jpowsour

A computationally efficient steady-state electrode-level and 1D + 1D cell-level fuel cell model

Cheng Bao [a,b,*], Wolfgang G. Bessler [b]

[a] Department of Thermal Science and Energy Engineering, School of Mechanical Engineering, University of Science & Technology Beijing, Beijing 100083, PR China
[b] German Aerospace Center (DLR), Institute of Technical Thermodynamics, Pfaffenwaldring 38-40, 70569 Stuttgart, Germany

ARTICLE INFO

Article history:
Received 23 December 2011
Received in revised form 5 March 2012
Accepted 7 March 2012
Available online 22 March 2012

Keywords:
Fuel cell
Modeling
Simulation
Approximation
Analytical model
Power-law approach

ABSTRACT

Computational efficiency is highly important for upscaling detailed electrode-level and cell-level models to the system level required for the design and control of fuel cells. We present a computationally efficient 1D + 1D fuel cell model based on a combination of analytical and numerical approaches. On the electrode level, we develop approximate analytical solutions for the 1D current/potential distribution via a hybrid algorithm of power-law approach and perturbation method. Compared to the conventional perturbation method, this work keeps the intrinsic nonlinearity of electrochemical kinetics, while providing clearer physical meaning than some purely mathematical methods like the Adomian decomposition method. By integrating the resulting overpotential profile into mass transfer models, concentration overpotentials are obtained and the thermodynamic framework is then used for analyzing the H_2/CO electrochemical co-oxidation kinetics. A novel expression is also presented to interconvert volume- and area-specific exchange current densities. On the cell level, a linear relationship between local current density and solid temperature is further developed for efficient 1D + 1D thermal along-the-channel numerical simulations without requiring computational iterations. Both the electrode-level and cell-level macroscopic fuel cell models are validated against full numerical solutions available in the open literatures over a wide range of operating conditions. With the hybrid analytical/numerical approximation in two dimensions, the computational framework is predicted to be sufficiently efficient for real-time simulations.

1. Introduction

Fuel cells are environmentally benign, high-efficiency energy conversion devices, and have been considered to be potential candidates for stationary power plants, automotive engines and portable applications. Modeling and simulation techniques are becoming increasingly important for both, understanding fundamental processes in fuel cells, and supporting design and optimization of fuel cell systems.

In recent years, many researchers have been developing multi-scale modeling frameworks of fuel cells [1–5]. Microscopic modeling aims at a physics-oriented explanation of the elementary kinetics of electrochemistry and transport, including its impedance-based analysis [6–8]. Macroscopic models have been developed for multi-dimensional, non-isothermal and transient simulation with computational fluid dynamics (CFD) based codes [9–11]. Although a direct combination of microscopic and macroscopic models would provide a better fundamental understanding of fuel cells, the complexity of both approaches makes it generally difficult to couple them into one single multi-scale model due to high numerical cost. On the other hand, simplified semi-empirical and analytical models are widely used in predicting polarization behavior of fuel cells [12,13]. However, the coarse framework and lacking of physical meaning limits their application, especially for spatially distributed modeling.

An accurate electrode-level and cell-level model with low computational cost is essential for system-level analysis, especially for controller design and hardware-in-the-loop simulations. Approximate analytical solutions provide a good balance between mechanistic and semi-empirical models. Gurau [14] presented an analytical solution of a transport model for polymer electrolyte membrane fuel cells (PEMFCs) with the assumption of constant overpotential in the catalyst layer. Considering the catalyst layer as an infinitely thin interface, Tsai [15] proposed a two-dimensional analytical expression of oxygen transport in the cathode diffusion layer of a PEMFC. Costamagna [16] obtained an analytical solution of overpotential distribution in solid oxide fuel cell (SOFC) electrodes by assuming constant gas concentration and exchange

* Corresponding author at: Department of Thermal Science and Energy Engineering, School of Mechanical Engineering, University of Science & Technology Beijing, Beijing 100083, PR China. Tel.: +86 10 62333682; fax: +86 10 62329145.
E-mail address: baocheng@mail.tsinghua.edu.cn (C. Bao).

0378-7753/$ – see front matter © 2012 Elsevier B.V. All rights reserved.
doi:10.1016/j.jpowsour.2012.03.023

Nomenclature

A	area (m^2)
$[A]$,$[B]$	matrixes of linear relationship, $[I]=[A][T_s]+[B]$
C	concentration ($mol\,m^{-3}$)
C_p	molar specific heat ($J\,mol^{-1}\,K^{-1}$)
D	diffusivity ($m^2\,s$) or channel depth (m)
F	Faraday's constant (96,487 $C\,mol^{-1}$)
H	molar enthalpy ($J\,mol^{-1}$)
i_0	volume-specific exchange current density ($A\,m^{-3}$)
I_0	area-specific exchange current density ($A\,m^{-2}$)
I	current density ($A\,m^{-2}$)
j	electrochemical reaction rate ($A\,m^{-3}$)
k_0	dimensionless variable in Eq. (3)
l	electrode thickness (m)
L	cell length (m)
n	power-law index or number of control volumes
n_e	electrons transferred per reacting molecule, $n_e=2$
N	flux ($mol\,m^{-2}\,s^{-1}$)
p	pressure (Pa)
r	volumetric reaction rate ($mol\,m^{-3}\,s^{-1}$)
R	universal gas constant ($8.314\,J\,mol^{-1}\,K^{-1}$) or reaction rate per area ($mol\,m^{-2}\,s^{-1}$)
S	molar entropy ($J\,mol^{-1}\,K^{-1}$)
T	temperature (K)
u	velocity ($m\,s^{-1}$)
W	width (m)
x	molar fraction or coordinate in thickness direction (m)
y	dimensionless overpotential, $y=n_eF\eta/RT$
z	coordinate in the cell length thickness (m)

Greek letters

α_a	anodic transfer coefficient
α_c	cathodic transfer coefficient
η	overpotential (V)
κ	heat conductivity ($W\,m^{-1}\,K^{-1}$)
ϕ	potential (V)
ρ	density ($kg\,m^{-3}$)
σ	conductivity ($S\,m^{-1}$)
υ	stoichiometric coefficient of reaction

Subscripts and superscripts

a	anode
c	cathode
e	electrolyte
eff	effective
el	electronic conducting phase
h	heat transfer
i, j	species
in	inlet
ion	ionic conducting phase
m	mass transfer
ref	reference or reforming reaction
s	solid phase
WGS	water gas shift reaction

current density. Considering variation of both gas concentration and overpotential, Bao [17] further proposed an approximate analytical solution of a transport model for anode-supported SOFCs. Other approximate analytical expressions were also developed for modeling channel flow and heat transfer in a fuel cell [18,19]. An overview of analytical fuel cell models is given in Kulikovsky's textbook [20].

This paper will firstly introduce a continuum transport model in porous electrodes of a fuel cell. Depending on the electrode thickness, different approximate analytical solutions of overpotential distribution, charge transfer, and electrochemical reaction are developed and then applied for modeling the mass transfer for various reactant systems. Finally, the 1D electrode model will be introduced into a numerical 1D along-the-channel cell-level model. An efficient computational framework is developed between the local current density and cell temperature. The models and results are discussed in the context of SOFCs, and are partly suitable for PEMFCs.

2. Background: electrode-level charge transport model

The core structure of a fuel cell is a "sandwich" configuration of the two electrodes and the membrane (membrane-electrode assembly, MEA). The electrodes of an SOFC, or the catalyst layers of a PEMFC, are formed by a mixture of an ionic (ion) conductor, an electronic (el) conductor, and pore space for gas diffusion, the connection of which make up three-phase boundary (TPB) regions. Close to the TPB, electrochemical reactions occur, exchanging electrical charges between ionic conducting phase and electronic conducting phase.

The model developed here is based on the following assumptions: the gas-phase is ideal, temperature and pressure are uniform throughout the electrode, both of the two conducting phases are continuous and homogeneous, and only steady state is considered. Furthermore, in order to decouple the problems of charge transfer and mass transfer for computational efficiency, we neglect the influence of gas concentration on the exchange current density and electrochemical reaction.

Along the positive direction from electrode/channel (E/C) interface to electrode/electrolyte (E/E) interface (x coordinate), according to Ohm's law, the charge transfer in two phases is

$$\nabla\cdot(-\sigma_{\mathrm{ion}}\nabla\phi_{\mathrm{ion}})=\nabla\cdot(\sigma_{\mathrm{el}}\nabla\phi_{\mathrm{el}})=j \tag{1}$$

where the ϕ and σ are the potential and conductivity, respectively, and the electrochemical reaction rate j can be described by a Butler–Volmer (BV) equation,

$$\begin{aligned} j &= i_0\left[\exp\left(\frac{\alpha_a n_e F}{RT}\eta\right)-\exp\left(-\frac{\alpha_c n_e F}{RT}\eta\right)\right]\\ i_0 &= i_{0,\mathrm{ref}}\exp\left[-\frac{E_{\mathrm{act}}}{R}\left(\frac{1}{T}-\frac{1}{T_{\mathrm{ref}}}\right)\right]\Pi\left(\frac{p_i}{p_0}\right)^{\nu_i}\end{aligned} \tag{2}$$

where F is the Faraday constant, R is the universal gas constant, T is the operating temperature, n_e is the number of electrons participating in the electrochemical reaction, α_a and α_c are the anodic and cathodic charge transfer coefficients, i_0 is the volume-specific exchange current density (which depends on both the TPB-specific exchange current density and the microstructure of the electrode), $i_{0,\mathrm{ref}}$ is the reference exchange current density at the reference temperature T_{ref}, E_{act} is the activation energy, p_i and ν_i are the partial pressure and reaction order of species i. The overpotential η is defined as the potential difference between the two phases $(\phi_{\mathrm{el}}-\phi_{\mathrm{ion}})$ minus that in equilibrium. At the E/C interface, the ionic current density completely transfers into the electronic current density, while at the E/E interface, the electronic current density completely transfers into the ionic current density.

The exchange current density i_0 depends on species concentration (last term in Eq. (2)), which is generally a function of position in the electrode thickness (here: x dimension) and along channel length (here: z dimension). In the present work, in order to derive computationally efficient analytical solutions, we assume that i_0 is constant through the electrode thickness and varies only along the channel length: the species bulk partial pressure at E/C interface $p_{i,\mathrm{b}}(z)$ rather than the TPB concentrations $p_i(x,z)$ is used in Eq. (2) for

the concentration-dependent exchange current density. Note that this assumption only influences the activation overpotential. The concentration overpotential is calculated using the fully resolved concentrations (Eq. (59)).

Define the following dimensionless variables

$$\zeta = \frac{x}{l}, \qquad y = f\eta, \qquad k_0 = \frac{i_0 f l^2}{\sigma_t} \tag{3}$$

where $f = n_e F/RT$, $\sigma_t = \sigma_{ion}\sigma_{el}/(\sigma_{ion}+\sigma_{el})$, l is the electrode thickness, ζ and y are dimensionless electrode thickness and overpotential, respectively, we obtain from Eqs. (1) and (2) the governing equation for overpotential distribution in a composite electrode,

$$\begin{cases} y'' = k_0[\exp(\alpha_a y) - \exp(-\alpha_c y)] \\ y'(\zeta=0) = N_0 = -\dfrac{Ifl}{\sigma_{el}}, \qquad y'(\zeta=1) = N_1 = \dfrac{Ifl}{\sigma_{ion}} \end{cases} \tag{4}$$

where I is the operating current density.

There are two main difficulties to solve this system analytically, one lies in the intrinsic equation structure related to the variable k_0, the other is the strong nonlinearity of exponent function. In addition, lacking of Dirichlet-type boundary conditions also brings some difficulties to this boundary-value problem, which will be explained later.

The variable k_0 is similar to the Thiele modulus for a classical problem of diffusion and reaction of gases throughout a porous catalyst pellet in isothermal conditions. In the present situation, low k_0 values mean that the electrode performance is kinetics-limited, whereas high k_0 values mean that the electrode performance is limited by the ionic conductivity. When k_0 is small enough ($k_0 \to 0$), the system reduces to a linear one, which does not satisfy the two Newman-type boundaries at the same time. When k_0 is big enough ($1/k_0 \to 0$), by multiplying $1/k_0$ at both sides of Eq. (4), the differential system reduces to an algebraic one, which means a strong boundary effect; this has been discussed in our previous work [17]. Because k_0 is proportional to l^2, both cases occur in practice due to the wide range of electrode size, e.g. the anode in anode-supported SOFC and the catalyst layer in PEMFC.

In literature [16,17,20], an exact solution of Eq. (4) has typically been obtained via linearization of the exponent, that is, by assuming that overpotentials are low. It results in

$$y_{lin} = \frac{N_1 - N_0 e^{-\lambda}}{\lambda(e^{\lambda} - e^{-\lambda})} e^{\lambda\zeta} + \frac{N_1 - N_0 e^{\lambda}}{\lambda(e^{\lambda} - e^{-\lambda})} e^{-\lambda\zeta}, \quad \lambda = \sqrt{k_0(\alpha_a + \alpha_c)} \tag{5}$$

Based on the singular perturbation method (SPM), we have previously obtained an approximate profile of overpotential, which consists of a logarithmic term due to mass transfer and two exponent terms due to boundary effects in a thick electrode [17]. When the variation of gas concentration is neglected (the logarithmic term vanishes), it reduces to

$$y_{spm} = \frac{N_1}{\lambda} e^{-\lambda(1-\zeta)} - \frac{N_0}{\lambda} e^{-\lambda\zeta} \tag{6}$$

Although this expression provides a relatively compact form and clearer physical meaning, it is almost numerically identical to Eq. (5) when $e^{-\lambda} \to 0$. Due to the inherent approximation of linearization the exponent term, both of them are inaccurate when the overpotential is not small. The key problem in this case is how to keep the nonlinearity of system.

3. Nonlinear approximation of the electrode-level model

3.1. Adomian decomposition method

The Adomian decomposition method (ADM) allows solution of nonlinear functional equations of various kinds (algebraic, differential, partial differential, integral, etc.) without approximating the operators [21]. For convenience to the reader, we briefly introduce the principle of ADM. Consider the generalized differential equation

$$Ly + Ry + Ny = g(\zeta) \tag{7}$$

where L is the highest order derivative, Ry is the linear differential operator of less order than L, Ny represents the nonlinear terms, and $g(\zeta)$ is the source term. Applying the inverse operator L^{-1} to both sides of Eq. (7), we obtain

$$y = f(\zeta) - L^{-1}(Ry) - L^{-1}(Ny) \tag{8}$$

where the function $f(\zeta)$ represents the terms arising from integrating $g(\zeta)$. Next, the nonlinear operator $Ny = F(y)$ is represented by an infinite series of the so-called Adomian polynomials

$$F(y) = \sum_{n=0}^{\infty} A_n \tag{9}$$

Define the solution $y(\zeta)$ by the series

$$y = \sum_{n=0}^{\infty} y_n \tag{10}$$

where the components y_n are determined recursively by the modified ADM [22]

$$\begin{aligned} &y_0 = f_0(\zeta), \\ &y_1 = f_1(\zeta) - L^{-1}(Ry_0) - L^{-1}(A_0), \\ &y_{k+2} = -L^{-1}(Ry_{k+1}) - L^{-1}(A_{k+1}), \quad k \geq 0 \end{aligned} \tag{11}$$

where $f(\zeta) = f_0(\zeta) + f_1(\zeta)$, and the Adomian polynomials are constructed by the following algorithm

$$A_n(y_0, y_1, \ldots, y_n) = \frac{1}{n!}\left[\frac{d^n}{d\lambda^n} F\left(\sum_{k=0}^{n} \lambda^k y_k\right)\right]_{\lambda=0} \tag{12}$$

In the fuel cell electrode model presented above (Eq. (4)), L is the 2nd-order differential and L^{-1} the two-fold integral, $Ry = 0$, $g(\zeta) = 0$ and $Ny = -k_0[\exp(\alpha_a y) - \exp(-\alpha_c y)]$. Therefore,

$$\begin{aligned} &y_0 = c_0, \\ &y_1 = -\frac{Ifl}{\sigma_{el}}\zeta + \frac{k_0}{2}(e^{\alpha_a c_0} - e^{-\alpha_c c_0})\zeta^2, \\ &y_2 = \frac{k_0}{6}(\alpha_a e^{\alpha_a c_0} + \alpha_c e^{-\alpha_c c_0})\left[-\frac{Ifl}{\sigma_{el}}\zeta^3 + \frac{k_0}{4}(e^{\alpha_a c_0} - e^{-\alpha_c c_0})\zeta^4\right], \ldots \end{aligned} \tag{13}$$

Substituting into Eq. (10), we obtain the ADM solution of overpotential, where the constant c_0 can be determined by the boundary condition, $dy/d\zeta\big|_{\zeta=1} = N_1$. Fig. 1 shows the comparison between the exact solution and ADM approximation with a different number of terms. With more terms, the ADM solution approaches gradually to the exact solution. When k_0 is not large, e.g. for the catalyst layer in PEMFC, ADM is an effective method for approximation. However, more terms are generally required to ensure accuracy, which leads a complicated expression without clear physical meaning. Furthermore, it is hard to obtain an explicit expression due to the implicit iteration of constant c_0. Under the condition of a large k_0 ($k_0 > 200$), for example, for anode-supported SOFCs, we found the ADM solution not satisfying and even not convergent.

3.2. Power-law approach

For thick electrodes, as present for example in anode-supported SOFCs, $1/k_0$ is small enough to be a perturbation variable [17], which can be applied to simplify the problem. Here, we employ a power function to approximate the exponential functions, that is,

$$e^{\alpha_a y} - e^{-\alpha_c y} = k(y + a)^n \tag{14}$$

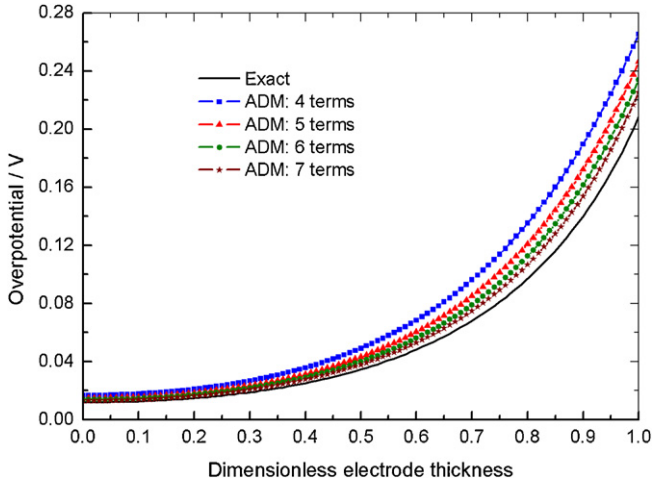

Fig. 1. Comparison between the exact solution and ADM solution with a different number of terms for parameters corresponding to an intermediate-temperature SOFC: $l = 50\,\mu m$, $\alpha_a = \alpha_c = 0.5$, $i_0 = 5 \times 10^8\,A\,m^{-3}$, $I = 4 \times 10^4\,A\,m^{-2}$, $T = 1073.15\,K$, $\sigma_{ion} = 2.267\,S\,m^{-1}$, $\sigma_{el} = 3.03 \times 10^4\,S\,m^{-1}$ and $k_0 = 11.93$.

where k, a, n are parameters to be determined later. Substituting into Eq. (4) yields

$$\begin{cases} y'' = k_0 k (y+a)^n \\ y'(1) = N_1 \end{cases} \xrightarrow{t=y+a} \begin{cases} t'' = k_0 k t^n \\ t'(1) = N_1 \end{cases} \tag{15}$$

The solution of the above system is a power-law expression, that is, $t = t(1)[1 + b(1-\zeta)]^m$. Substituting into Eq. (15), we obtain $m = 2/(1-n)$ and

$$\begin{aligned} &\frac{b^2}{k} = \frac{k_0 (1-n)^2}{2(1+n)} [y(1)+a]^{n-1} \\ &-2b[y(1)+a] = (1-n)N_1 \end{aligned} \tag{16}$$

In order to obtain values for the coefficients, both the zero-order and first-order differential of the power function approach is set to that of the corresponding full exponential expression at the E/E interface.

$$\begin{aligned} f_1 &= e^{\alpha_a y(1)} - e^{-\alpha_c y(1)} = k[y(1)+a]^n \\ f_2 &= \alpha_a e^{\alpha_a y(1)} + \alpha_c e^{-\alpha_c y(1)} = nk[y(1)+a]^{n-1} \end{aligned} \tag{17}$$

The explicit expressions of n, a, k, b can be solved from Eqs. (16) and (17)

$$\begin{aligned} n &= \frac{f_2 N_1^2}{2k_0 f_1^2 - f_2 N_1^2}, \qquad a = \frac{f_1 N_1^2}{2k_0 f_1^2 - f_2 N_1^2} - y(1), \\ k &= \frac{f_1}{(f_1 N_1^2/(2k_0 f_1^2 - f_2 N_1^2))^n}, \qquad b = -\frac{2N_1(2k_0 f_1^2 - f_2 N_1^2)}{(1-n) f_1 N_1^2} \end{aligned} \tag{18}$$

In order to determine $y(1)$, we reenter into the original system of Eq. (4) to obtain an exact implicit solution

$$(y')^2 = 2k_0 \left(\frac{1}{\alpha} e^{\alpha_a y} + \frac{1}{\beta} e^{-\alpha_c y} + C \right) \tag{19}$$

As mentioned above, lacking Dirichlet-type boundary condition brings difficulty to determine the constant C. Considering the sign of 1st- and 2nd-order derivatives at the electrode boundaries ($d^2y > 0$, $dy(0) < 0$, $dy(1) > 0$), the solution should show a concave profile. For a thick electrode, most of the electrode is inactive to electrochemical reaction, which means at the minimum point

$$y' = 0, \qquad y \approx 0 \tag{20}$$

Therefore, $C = -(1/\alpha_a + 1/\alpha_c)$, and the overpotential at the E/E interface $y(1)$ can be solved by

$$2k_0 \left(\frac{1}{\alpha_a} e^{\alpha_a y(1)} + \frac{1}{\alpha_c} e^{-\alpha_c y(1)} - \frac{1}{\alpha_a} - \frac{1}{\alpha_c} \right) = N_1^2 \tag{21}$$

When $\alpha_a = \alpha_c$, there is an exact solution

$$y(1) = \frac{1}{\alpha_a} \ln \left(\frac{1}{2} \left[\frac{\alpha_a N_1^2}{2k_0} + 2 + \sqrt{\left(\frac{\alpha_a N_1^2}{2k_0} + 2 \right)^2 - 4} \right] \right) \tag{22}$$

Thus, we get an explicit power function which is valid in the region close to the E/E interface

$$y_{p1} = [y(1) + a][1 + b(1-\zeta)]^{2/(1-n)} - a \tag{23}$$

The power function close to the E/C boundary can be obtained similarly and is given by

$$y_{p0} = [y(0) + a'][1 - b'\zeta]^{2/(1-n')} - a' \tag{24}$$

where a', b', n', $y(0)$ are calculated by replacing N_1, $y(1)$ to N_0, $y(0)$ in all the related equations.

3.3. Hybrid power law and linear approximation

The power law approximation as derived above is valid only in the region close the electrode interfaces. On the other hand, the linear approximation (Eq. (5)) should be valid in most of the region in a thick electrode due to a small electrochemical reaction rate. Therefore, we propose a hybrid function to make a smooth transition between these two expressions.

Based on the analysis of boundary-layer effect in our previous work [17], we construct

$$y = y_{lin,WKB} + (y_{p1} - y_{lin,WKB}) e^{-s_0 \lambda (1-\zeta)} + g_1(\zeta) \tag{25}$$

where

$$\begin{aligned} y_{lin,WKB} &= \frac{(N_1 - N_0 e^{-s_0\lambda}) e^{s_0\lambda\zeta} + (N_1 - N_0 e^{s_0\lambda}) e^{-s_0\lambda\zeta}}{s_0\lambda (e^{s_0\lambda} - e^{-s_0\lambda})}, \\ s_0 &= \sqrt{\frac{e^{\alpha_a} - e^{-\alpha_c}}{\alpha_a + \alpha_c}} \end{aligned} \tag{26}$$

Here, we apply an additional correction to the linear approximation (Eq. (5)) based on the WKB (Wentzel, Kramers and Brillouin) perturbation method [23], which is explained in detail in Appendix A. In order to make y strictly satisfy the boundary conditions in Eq. (4), $g_1(\zeta)$ is added and derived by considering the requirements

$$\begin{aligned} &g_1(0) = 0, \qquad g_1'(0) = 0, \qquad g_1(1) = 0, \\ &g_1'(1) = -s_0\lambda [y_{p1}(1) - y_{lin,WKB}(1)] \end{aligned} \tag{27}$$

yielding

$$g_1(\zeta) = s_0\lambda [y_{p1}(1) - y_{lin,WKB}(1)] \zeta (1-\zeta) e^{-s_1\lambda(1-\zeta)} \tag{28}$$

In principle, the slope rate s_1 should be fitted from the exact numerical solution. However, we tried to simply chose $s_1 = 1.3 s_0$, which is satisfying enough in a wide range of applications.

The final approximation solution using the hybrid power-law and linearization approach is

$$\begin{aligned} y = {} & y_{lin,WKB} + (y_{p1} - y_{lin,WKB}) e^{-s_0\lambda(1-\zeta)} + s_0\lambda [y_{p1}(1) - y_{lin,WKB}(1)] \\ & \zeta(1-\zeta) e^{-s_1\lambda(1-\zeta)} + (y_{p0} - y_{lin,WKB}) e^{-s_0\lambda\zeta} + s_0\lambda [y_{p0}(0) \\ & - y_{lin,WKB}(0)] \zeta (1-\zeta) e^{-s_1\lambda\zeta} \end{aligned} \tag{29}$$

In practical fuel cells, the electronic conductivity is generally much larger than the ionic conductivity ($\sigma_{ion} \ll \sigma_{el}$), the boundary

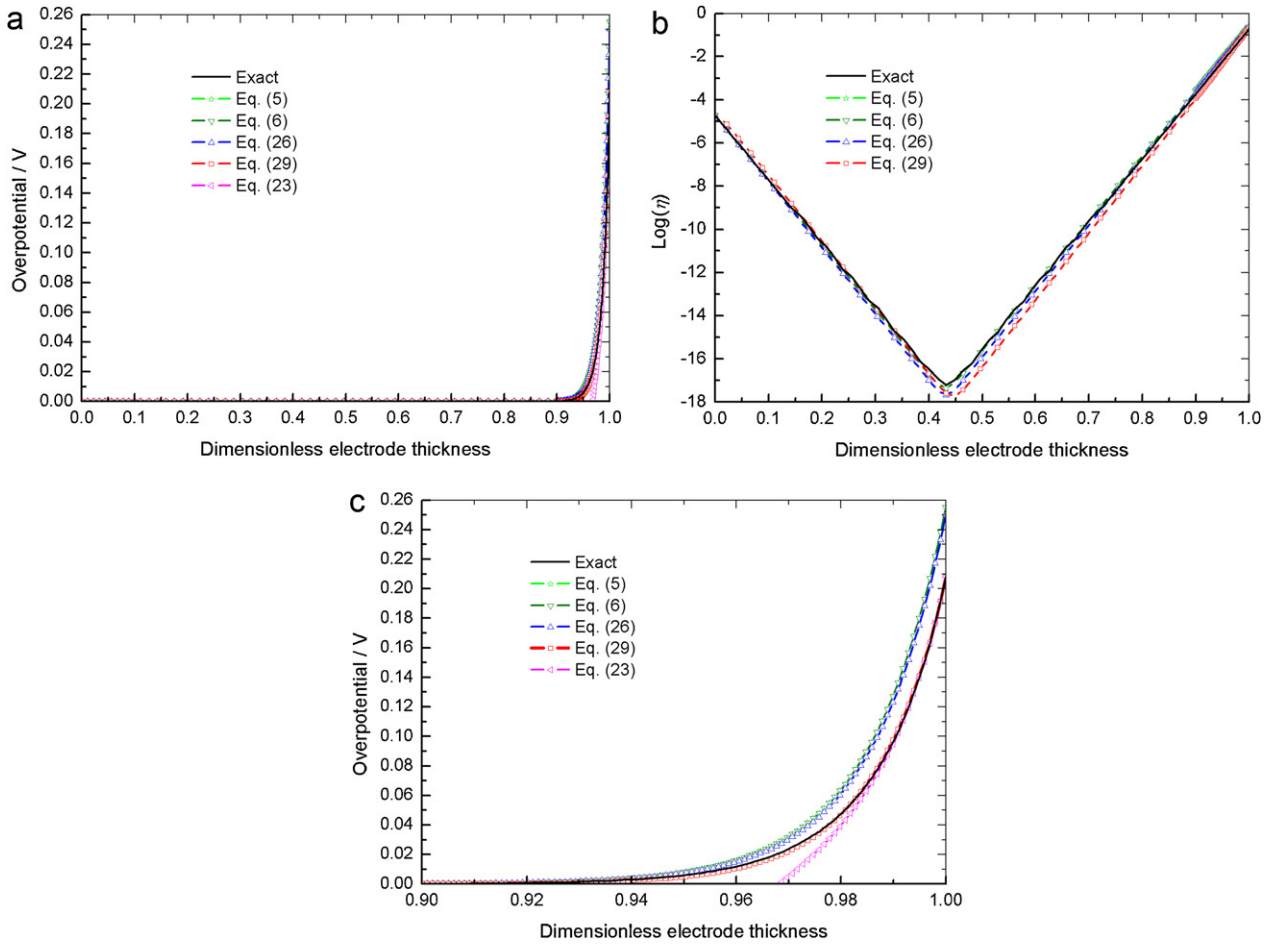

Fig. 2. Comparison between the exact solution and different approximation solutions for parameters corresponding to an anode-supported SOFC: $l = 1$ mm, $\alpha_a = \alpha_c = 0.5$, $i_0 = 5 \times 10^8$ A m^{-3}, $I = 4 \times 10^4$ A m^{-2}, $T = 1073.15$ K, $\sigma_{ion} = 2.267$ S m^{-1}, $\sigma_{el} = 3.03 \times 10^4$ S m^{-1} and $k_0 = 4771$. (a) Linear presentation of overpotential as function of electrode thickness, (b) logarithmic presentation of the same data, and (c) linear presentation of the region close to E/E interface.

effect at the E/C interface is negligible and only the first three terms in Eq. (29) are needed.

For a typical anode-supported SOFC, Fig. 2(a) shows the overpotential profiles calculated via the exact numerical solution, linear approximation in Eq. (5), SPM approximation in Eq. (6), WKB approximation in Eq. (26), hybrid power-law approximation in Eq. (29) and the power function in Eq. (23). All the overpotential profiles show a strong boundary-layer effect due to a large k_0. For a clearer image, Fig. 2(b) and (c) further shows the logarithmic or linear overpotential profile within the whole electrode or the region close to the E/E interface. The linear and SPM approximations are almost overlapping as mentioned before. Note that although starting from the assumption of a thick electrode, the power-law approach is found to be accurate as $k_0 > 20$, which corresponds to an electrode thickness of around 60 μm assuming other typical parameters. Fig. 3 shows the effect of the operating current density on the index of power function. As current density decreases, the power-law index approaches gradually to unity, which means a linear approximation. Fig. 4(a) and (b) respectively shows the linear- and logarithmic-type exact and power-law solutions when the electronic conductivity is equal to the ionic conductivity ($\sigma_{ion} = \sigma_{el}$). Such a situation is present in the so-called IDEAL-cell concept [24], as a result, all the five terms in Eq. (29) are necessary, thus the boundary-layer effects at both sides of electrode can be accurately reflected by the power-law approximation. Due to analytical expression, the hybrid power-law and linear approximation is smoother than the exact numeric solution with 250 finite-difference discrete grids.

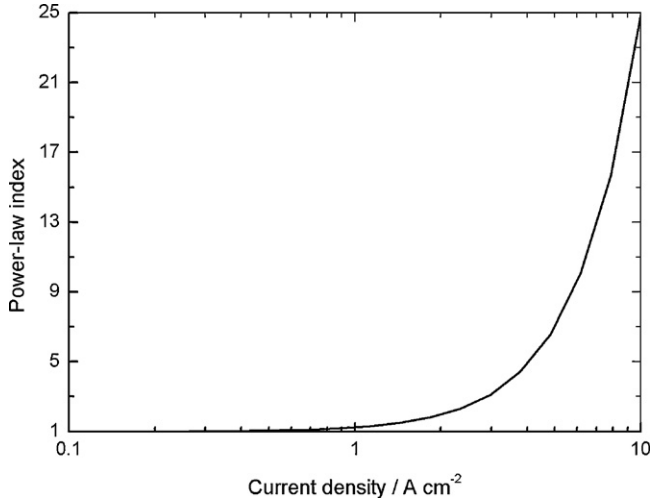

Fig. 3. Index of the power function (Eq. (14)) as function of the operating current density, other parameters are identical to those in Fig. 2.

3.4. Relationship between volume-specific and area-specific exchange current densities

In the above electrode model, electrochemical reactions are assumed to occur throughout the complete thickness of the porous

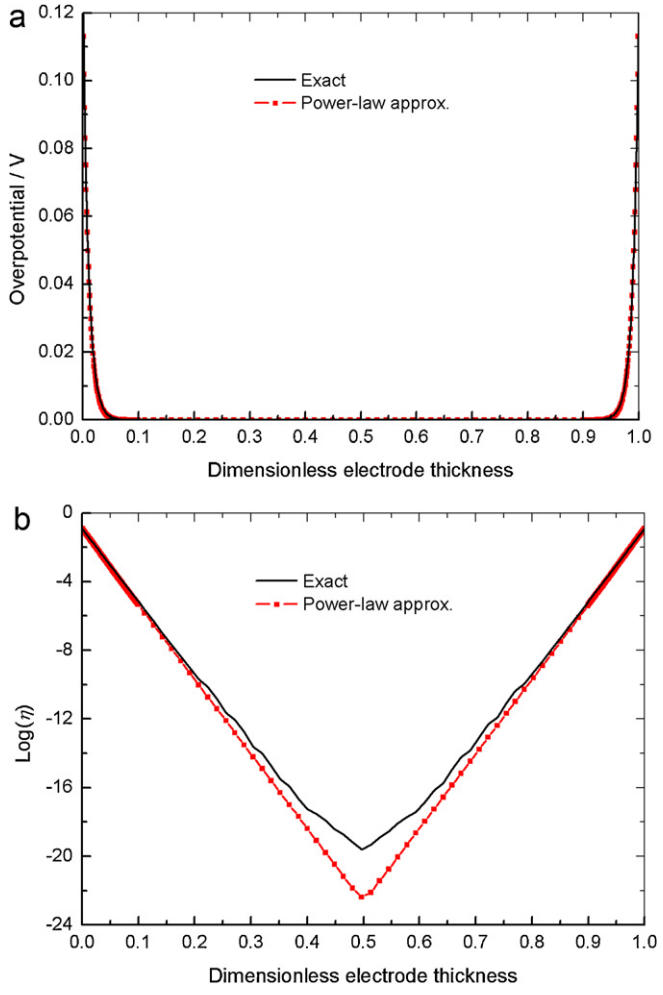

Fig. 4. Comparison between the exact solution and power-law approximation for $\sigma_{el} = \sigma_{ion}$ and $I = 3 \times 10^4$ A m^{-2}, other parameters are identical to those in Fig. 2. (a) Linear and (b) logarithmic presentation.

electrode (volumetric model). The exchange current density i_0 is a volume-specific parameter (given in Ampere per electrode volume). On the other hand, many models in literature assume that electrochemistry takes only place at the E/E interface (interfacial model). The exchange current density used in those models is an area-specific parameter (given in Ampere per cell area), that is,

$$I = I_0[\exp(\alpha_a f\eta_{act}) - \exp(-\alpha_c f\eta_{act})] \tag{30}$$

where η_{act} is the total activation overpotential, I_0 the area-specific exchange current density.

Eq. (19) provides an exact solution of the overpotential at the E/E interface, $\eta_{E/E}$. As $\sigma_{ion} \ll \sigma_{el}$, $\eta_{E/E}$ is almost equal to the total activation overpotential (refer to Eq. (59)). Due to equivalence of these two modeling approaches, $\eta_{act} = \eta_{E/E}$, a relationship between volume-specific and area-specific exchange current densities can be derived. For $\alpha_a = \alpha_c$,

$$i_0 = \frac{a_a\sigma_t f I^2}{2\sigma_{ion}^2\left(\sqrt{(I^2/I_0^2)+4} + a_a C\right)} \tag{31}$$

For a thick electrode (Eq. (20) is valid), $\alpha_a C = -2$. Expand the square root term based on the binomial theorem as generally $(I/I_0)^2 \ll 1$, we obtain an expression independent of the operation current density

$$i_0 = \frac{2I_0^2 a_a\sigma_t f}{\sigma_{ion}^2} \approx \frac{2I_0^2 a_a f}{\sigma_{ion}} \tag{32}$$

This expression shows a nonlinear relationship between these two exchange current densities, which is different to the common relationship with a simple geometric factor, $i_0 = I_0 f_{geo}$, which we believe lacks theoretical support.

4. Integration of mass transfer into electrode-level model

The model presented in the sections above treats charge transfer only. Here, we add expressions for mass transfer. Note that, in order to decouple mass and charge transport formulations, the influence of concentration on exchange current density is neglected in this work. The mass transfer of multi-component gas species in a porous electrode is governed by the Stefan–Maxwell equations,

$$\nabla x_i = \sum_{j \neq i} \frac{x_i N_j - x_j N_i}{cD_{ij,eff}} \tag{33}$$

where c is the concentration of gas mixture, $x_i = c_i/c_t$ and N_i are the molar fraction and flux of species i, respectively, $D_{ij,eff}$ is the effective diffusivity, which includes the binary diffusivity between species i and j (D_{ij}) and their Knudsen diffusion coefficients ($D_{i,K}$, $D_{j,K}$) and is corrected by the electrode porosity (ε) and tortuosity (τ) as [2]

$$D_{ij,eff} = \frac{\varepsilon}{2\tau^2}\left[\frac{1}{(1/D_{ij})+(1/D_{i,K})} + \frac{1}{(1/D_{ij})+(1/D_{j,K})}\right],$$

$$D_{i,K} = \frac{2}{3} r_P \sqrt{\frac{8RT}{\pi M_i}} \tag{34}$$

where r_P is the average particle size of electrode and M_i is the molecular weight of species i.

The mass balance of species i is given by

$$\nabla \cdot (N_i) = \frac{\upsilon_i j}{n_e F} + \sum_k \upsilon_{i,k} r_k \tag{35}$$

where υ_i, $\upsilon_{i,k}$ are the stoichiometric coefficients of species i in the electrochemical reaction and in chemical reaction k (e.g., reforming reaction and water gas shift reaction), respectively.

As boundary conditions, the species concentration at the E/C interface is assumed to be equal to the bulk channel concentration, and at the E/E interface, the species can not penetrate the dense electrolyte layer (note this assumption is not correct for PEMFCs, where there is complex water management in the PEM), that is, $x_i(x=0) = x_{i,b}$, $N_i(x=l) = 0$.

4.1. H_2–H_2O or CO–CO_2 system

In this binary stationary system (1: H_2, 2: H_2O), equimolar counter diffusion occurs ($N_1 = -N_2$) and there are no chemical reactions, that is, $dN_1/dx = \upsilon_1 j/n_e F$ or $d^2x_1/dx^2 = -\upsilon_1 j/cD_{12,eff} n_e F$. Because $d^2\eta/dx^2 = j/\sigma_t$, there is a simple relationship between the profiles of gas concentration and overpotential

$$x_1(x) = x_{1,b} - \frac{\upsilon_1\sigma_t}{cD_{12,eff}n_e F}\left[\eta(x) - \eta(0) - \frac{I}{\sigma_{ion}}x\right] \tag{36}$$

where $\eta(x)$ has been determined from the power-law approach.

4.2. H_2–H_2O–N_2 or CO–CO_2–N_2 system

In this case (1: H_2, 2: H_2O, 3: N_2), N_2 is inert ($N_3 = 0$, note that we investigate the stationary case only) and H_2-H_2O shows an equimolar counter diffusion ($N_1 = -N_2$), i.e. $d^2(\ln x_3)/dx^2 = \upsilon_1 j(1/D_{13,\text{eff}} - 1/D_{23,\text{eff}})/cn_eF$. So,

$$x_3(x) = x_{3,\text{b}} \exp\left(\frac{\sigma_\text{t}\upsilon_1}{cn_eF}\left(\frac{1}{D_{13,\text{eff}}} - \frac{1}{D_{23,\text{eff}}}\right)\left[\eta(x) - \eta(0) - \frac{I}{\sigma_\text{ion}}x\right]\right) \tag{37}$$

$$x_1(x) = x_{1,\text{b}} - \frac{D_{23,\text{eff}}[D_{13,\text{eff}}\ln(x_3/x_{3,\text{b}}) + (D_{12,\text{eff}} - D_{13,\text{eff}})(x_3 - x_{3,\text{b}})]}{D_{12,\text{eff}}(D_{23,\text{eff}} - D_{13,\text{eff}})} \tag{38}$$

When $x_{3,\text{b}} = 0$, Eq. (38) reduces to Eq. (36) automatically.

4.3. O_2–N_2 system

Consider N_2 is inert ($N_2 = 0$), that is, $d^2(\ln x_2)/dx^2 = \upsilon_1 j/cD_{12,\text{eff}}n_eF$. Therefore,

$$x_2(x) = x_{2,\text{b}} \exp\left(\frac{\upsilon_1\sigma_\text{t}}{cD_{12,\text{eff}}n_eF}\left[\eta(x) - \eta(0) - \frac{I}{\sigma_\text{ion}}x\right]\right) \tag{39}$$

4.4. O_2–N_2–H_2O system

It is a typical case in cathode catalyst layer of PEMFC (1: O_2, 2: N_2, 3: H_2O). Assume the net water and gas-species flux via the membrane is zero for simplicity, that is, N_2 is inert ($N_2 = 0$) and O_2–H_2O flux are related to as $N_1/\upsilon_1 = N_3/\upsilon_3$. So, $d^2(\ln x_2)/dx^2 = (\upsilon_1/D_{12,\text{eff}} + \upsilon_3/D_{23,\text{eff}})j/cn_eF$, which leads to

$$x_2(x) = x_{2,\text{b}} \exp\left(\frac{\sigma_\text{t}}{n_eF}\left(\frac{\upsilon_1}{cD_{12,\text{eff}}} + \frac{\upsilon_3}{cD_{23,\text{eff}}}\right)\left[\eta(x) - \eta(0) - \frac{I}{\sigma_\text{ion}}x\right]\right) \tag{40}$$

$$x_1(x) = \left(x_{1,\text{b}} - \frac{\upsilon_1}{\upsilon_1 + \upsilon_3} + \frac{ax_{2,\text{b}}}{m-1}\right)\left(\frac{x_2}{x_{2,\text{b}}}\right)^m + \frac{\upsilon_1}{\upsilon_1 + \upsilon_3} - \frac{a}{m-1}x_2 \tag{41}$$

where

$$m = \frac{(\upsilon_1 + \upsilon_3)D_{23,\text{eff}}D_{12,\text{eff}}}{D_{13,\text{eff}}(\upsilon_1 D_{23,\text{eff}} + \upsilon_3 D_{12,\text{eff}})}, \qquad a = \frac{\upsilon_1 m}{\upsilon_1 + \upsilon_3}\left(1 - \frac{D_{13,\text{eff}}}{D_{12,\text{eff}}}\right) \tag{42}$$

4.5. H_2–H_2O–CO–CO_2–N_2 system

Instead of the Stefan–Maxwell equation, we use Fick's law for this case to describe the multi-component (1: H_2, 2: H_2O, 3: CO, 4: CO_2, 5: N_2) mass transfer using a simple analytical solution, that is,

$$N_i = -cD_i\frac{dx_i}{dz} + x_i\sum_{j=1}^{5}N_j \quad (i = 1, 2, 3, 4) \tag{43}$$

where D_i is the Fick diffusivity of species i, which is considered constant for simplicity. Because Fick's law is not strictly valid for multi-component transport, N_2 is treated here as a balancing species, that is, the above equation is not used for N_2 and the N_2 molar fraction (x_5) follows from $\sum x_i = 1$.

Consider electrochemical oxidations of both H_2 and CO,

$$\frac{dN_1}{dx} = -\frac{dN_2}{dx} = -\frac{\omega j}{n_eF} + r_\text{WGS}, \qquad \frac{dN_3}{dx} = -\frac{dN_4}{dx} = -\frac{(1-\omega)j}{n_eF} - r_\text{WGS} \tag{44}$$

where ω is the proportion of H_2 electrochemical current density in the total current density, $\omega = j_{H_2}/(j_{H_2} + j_\text{CO})$, and r_WGS is the rate of the water-gas shift reaction ($\text{CO} + \text{H}_2\text{O} \rightleftarrows \text{CO}_2 + \text{H}_2$), which is considered as the only chemical reaction in this paper. Note that in the present work we neglect carbon formation (e.g., due to Boudouard reaction); also, because no CH_4 is assumed present, there are no steam reforming or dry reforming reactions.

At the E/E interface, fluxes of all the species are zero ($N_i\big|_{x=l} = 0$), which leads to $N_1 = -N_2$, $N_3 = -N_4$, $\sum N_i = 0$, $dN_1/dx + dN_3/dx = -cD_1d^2x_1/dx^2 - cD_3d^2x_3/dx^2 = -j/n_eF$. Therefore,

$$D_1x_1 + D_3x_3 = \frac{\sigma_\text{t}}{cn_eF}\eta - \frac{\sigma_\text{t}I}{cn_eF\sigma_\text{ion}}x + a = f(x) \tag{45}$$

$$D_1x_1 + D_2x_2 = D_1x_{1,\text{b}} + D_2x_{2,\text{b}}, \qquad D_3x_3 + D_4x_4 = D_3x_{3,\text{b}} + D_4x_{4,\text{b}} \tag{46}$$

where $a = D_1x_{1,\text{b}} + D_3x_{3,\text{b}} - \sigma_\text{t}\eta(0)/cn_eF$. Assume the water-gas shift reaction is in thermodynamic equilibrium ($r_\text{WGS} = 0$), i.e.

$$x_1x_4 = K_\text{shift}x_2x_3 \tag{47}$$

where K_shift is the equilibrium constant of water shift reaction, we obtain the concentration distribution of species from Eqs. (45)–(47),

$$x_1(x) = \frac{b(x) - \sqrt{b^2(x) - 4k(k-1)(D_1x_{1,\text{b}} + D_2x_{2,\text{b}})f(x)}}{2D_1(k-1)} \tag{48}$$

where $k = K_\text{shift}D_1D_4/D_2D_3$ and

$$b(x) = (k-1)f(x) + k(D_1x_{1,\text{b}} + D_2x_{2,\text{b}}) + D_3x_{3,\text{b}} + D_4x_{4,\text{b}} \tag{49}$$

The concentrations of other species can be obtained by substituting x_1 into Eqs. (45) and (46). Like the other cases mentioned above, the profile of gas concentrations can be used to calculate the concentration loss and limiting current density based on Fick's law.

More importantly, an analytical expression of the proportion of H_2 electrochemical current density is available from the explicit profiles of H_2 concentration and overpotential, that is,

$$\omega(x) = \frac{(cD_1n_eF/\sigma_t)(d^2x_1/dx^2)}{(d^2\eta/dx^2)} \tag{50}$$

For analysis of H_2 and CO electrochemical co-oxidation, generally different exchange current densities are used for H_2 and CO, but the uncertainties of these kinetic data are currently under wide discussion. On the other hand, because the water gas shift reaction (WGSR) is fast and usually assumed to be in equilibrium, it is not possible to separate the different exchange current densities from an analysis of gas concentrations only. Still, the present framework, resulting in Eq. (50), provides some information for kinetic analysis. Here, the unique exchange current density can be explained as a global or overall one corresponding to the overall overpotential driving both H_2 and CO oxidation. Fig. 5 shows the proportion of H_2 electrochemical current density in the total current density, ω, in the active zone under the conditions of different fuel compositions. The active zone is also called boundary layer of electrochemical reaction, where 99% variation of the ionic current density occurs

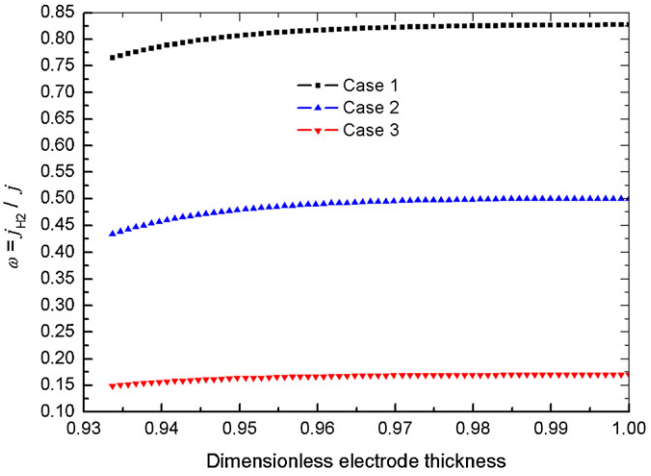

Fig. 5. Ratio of H_2 over the total electrochemical current density in the active zone for different fuel composition of case 1: 31.77% H_2–18.23% H_2O–28.23% CO–16.77% CO_2–5% N_2, $I = 2 \times 10^4$ A m^{-2}, case 2: 22.24% H_2–7.76% H_2O–47.76% CO–17.24% CO_2–5% N_2, $I = 1 \times 10^4$ A m^{-2}, case 3: 8.98% H_2–1.02% H_2O–76.02% CO–8.98% CO_2–5% N_2, $I = 0.5 \times 10^4$ A m^{-2}, and the other parameters are the same as those in Fig. 2.

[17]. It is obvious that the fuel composition has a great influence on the electrochemical kinetics of H_2 and CO. As CO concentration increases or H_2 concentration decreases, ω decreases. However, when the concentrations of H_2 and CO are comparable, most of electrochemical current density (over 80% in case 1) results from oxidation of H_2.

5. Along-the-channel cell-level model

The approximate analytical solution of electrode-level model derived above is further integrated into a 1D thermal cell-level model where transport of mass and heat along a single channel is considered. This yields an overall 1D + 1D model, where the dimension x through the MEA is solved analytically and the dimension z along the channel length is solved numerically. Only steady state is considered here.

5.1. Governing equations and background

Along the coordinate of channel length, $z \in [0, L]$, the gas-phase energy balance, species and overall mass balance are given by [4]

$$c_k u_k C_{p,k} \frac{\partial T_k}{\partial z} = Q_k \quad (k = a, c) \tag{51}$$

$$\frac{\partial (c u x_i)_k}{\partial z} = S_{m,k}(-\xi_{rib} N_{i,E/C} + \upsilon_{i,ref} R_{ref} + \upsilon_{i,WGS} R_{WGS})_k \tag{52}$$

$$\frac{\partial (cuT)_k}{\partial z} = T_k S_{m,k} \sum_i (-\xi_{rib} N_{i,E/C} + \upsilon_{i,ref} R_{ref} + \upsilon_{i,WGS} R_{WGS})_k + \frac{Q_k}{C_{p,k}} \tag{53}$$

Here, Eq. (53) is a combination of the total mass balance and the ideal gas law, $p = cRT$, so $\partial p/\partial t = R(T\partial c/\partial_t + c\partial T/\partial t)$. Substituting Eqs. (51) and (52) to this expression, one will find that there is no transient term (even for transient simulation) when not considering the pressure dynamics ($\partial p/\partial t = 0$, $\partial p/\partial z$ is not forcedly excluded). The advantage of this formulation is to provide an equation with gas velocity included as dependent variable, as we do not put forward the complex momentum equation (like in the full Navier–Stokes equations). This treatment has been shown before to be numerically much more stable than the direct use of the ideal gas law [4], and can be also found in Heidebrecht's work [25].

The heat source is given by

$$Q_k = S_{h,k} h_k (T_s - T_k) + S_{m,k} \left[-\sum_i (\upsilon_{i,ref} H_{i,a} R_{ref} + \upsilon_{i,WGS} H_{i,a} R_{WGS}) + \sum_i \max(-\xi_{rib} N_{i,E/C}, 0) C_{p,i} (T_s - T) \right]_k \tag{54}$$

where T_a, T_c, T_s are temperature of the anode gas, cathode gas and solid matrix, u is the gas velocity, h is the convective heat transfer coefficient, x_i, $C_{p,i}$ and H_i are the molar fraction, molar specific heat and enthalpy of species i, $C_p = \sum_i C_{p,i} x_i$ is the gas molar specific heat. For rectangular flow channels in a typical planar SOFC, the specific mass transfer area (S_m) and heat transfer area (S_h) per unit volume of flow channel and rib coefficient (ξ_{rib}) are

$$S_{m,k} = \frac{1}{D_{ch,k}}, \qquad S_{h,k} = \frac{2(D_{ch,k} + W_{ch})}{D_{ch,k} W_{ch}}, \qquad \zeta_{rib} = 1 + \frac{W_{rib}}{W_{ch}} \tag{55}$$

where D_{ch}, W_{ch} are the depth and width of flow channel and W_{rib} is the rib width.

For the solid-phase energy balance it is assumed that temperature varies only in z direction, while in x direction all solid components (MEA and interconnectors) have the same temperature. Radiant heat transfer is neglected. The energy balance is given by

$$\kappa_s \frac{\partial^2 T_s}{\partial z^2} = \sum_{k=a,c} \gamma_k \xi_{rib} S_{m,k} \sum_i N_{i,E/C} H_{k,i}(T_k, T_s) - \sum_{k=a,c} \gamma_k S_{h,k} h_k (T_k - T_s) + \gamma_c \xi_{rib} S_{m,c} I(z) V_{cell} \tag{56}$$

where κ_s is heat conductivity, $\gamma_k = D_{ch,k} W_{ch} / (A_{con,a} + A_{con,c} + l_{MEA} W_{ch})$ the ratio of solid-phase heat conduction area to gas-phase mass or heat transfer area, where l_{MEA} is the MEA thickness, A_{con} the section area of interconnector.

The cell voltage, V_{cell}, which is assumed constant along the channel (ideal conductivity of the interconnectors), can be obtained by

$$V_{cell} = V_{oc}(z) - \eta_{t,a}(z) - \eta_{t,c}(z) - \frac{I(z) l_e}{\sigma_{ion}} \tag{57}$$

where $I(z)$ is the local cell-area-specific current density, l_e the thickness of the electrolyte layer, the local open circuit voltage, V_{oc} is calculated by the Nernst equation

$$V_{oc} = E_{0,ref} + \frac{\Delta S_{ref}}{n_e F}(T_s - T_{ref}) + \frac{RT}{n_e F} \ln \frac{x_{H2,b} (p_c x_{O2,b} / p_0)^{0.5}}{x_{H2O,b}} \tag{58}$$

where $E_{0,ref}$, ΔS_{ref} are the reference electromotive force and entropy change of the overall electrochemical reaction (here: $H_2 + 0.5O_2 \rightarrow H_2O$), and the total overpotential everywhere along the channel, $\eta_t(z)$ can be obtained from the approximation solution $\eta(z,x)$ and $x_i(z,x)$ of the local electrode-level model via

$$\eta_t(z) = \frac{1}{\sigma_{el} + \sigma_{ion}} [\sigma_{ion} \eta(z, 0) + \sigma_{el} \eta(z, l) + I(z) l] + \frac{RT}{n_e F} \ln \frac{x_i(z, l)}{x_i(z, 0)} \tag{59}$$

The overall equation system represents the implicit relationship between cell voltage V_{cell} and average cell current density I_{cell}. Either can be independently specified, and the other value is simulated. The fuel cell is generally treated as a set of parallel discrete elements with uniform cell voltage and non-uniform local current densities. Thus, as shown in Fig. 6, a high-level iteration loop is required for the cell voltage or average current density. This iteration loop greatly increases the computational cost and also the risk of numerical divergence, although this problem can be alleviated by equation-oriented solvers like gPROMS [4].

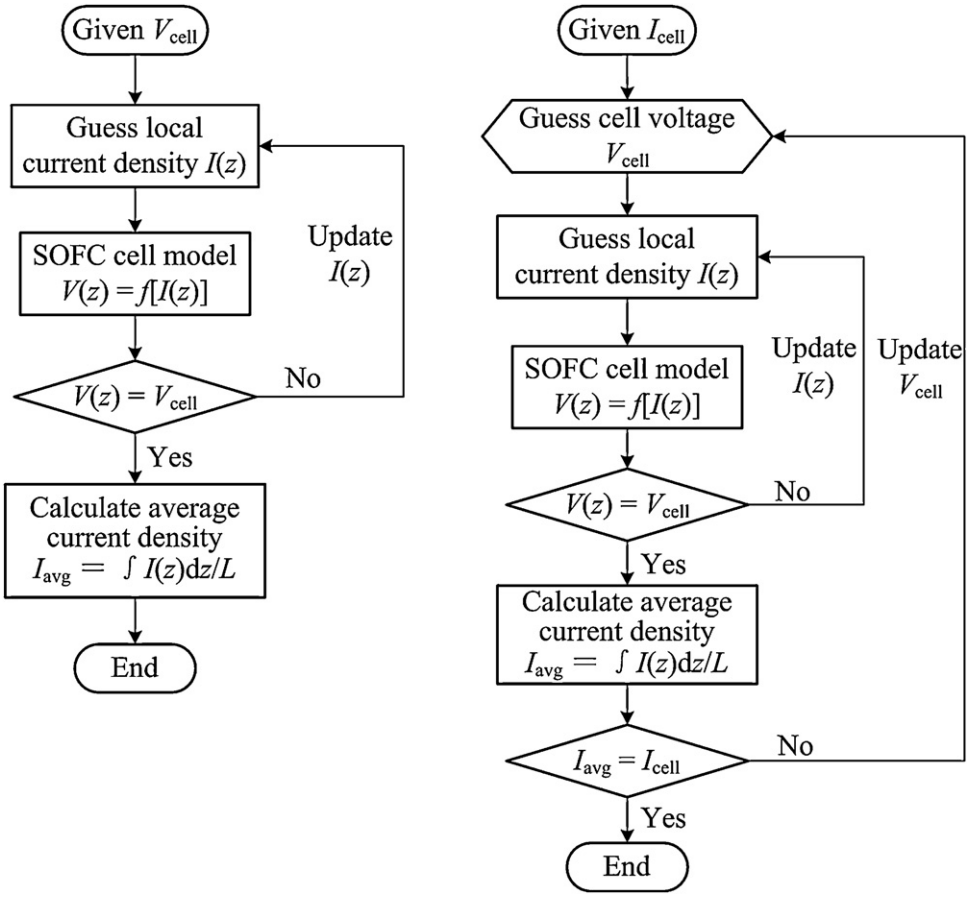

Fig. 6. Flow chart of voltage–current iteration loop in distributed fuel cell modeling.

5.2. Discrete form and model simplification

Assuming that the total gas pressure, gas molar specific heat, and electrochemical reaction heat (ΔH) are constant, we further simplify the computational framework of distributed modeling. For the simplest case in SOFCs, that is, H_2/H_2O at the anode and O_2/N_2 at the cathode, $R_{ref} = R_{WGS} = 0$, $N_{i,E/C} = -\upsilon_i I(z)/n_e F$, $c_a u_a = c_{a,in} u_{a,in}$, and the variation of total gas molar flux in the cathode flow channel is considered negligible ($c_c u_c = c_{c,in} u_{c,in}$) due to a generally large stoichiometry of O_2 and dilute effect of N_2. Based on the control-volume discretization approach as shown in Fig. 7, we can obtain the following discrete forms according to the power law or the upwind scheme [26].

For co-flow,

$$T_{a,j} \approx aT_{a,j-1} + (1-a)T_{s,j}, \qquad T_{c,j} = bT_{c,j-1} + (1-b)T_{s,j} \quad (j = 2, \ldots, n+1) \tag{60}$$

$$x_{H2,j} = x_{H2,j-1} + k_{H2} I_{j-1}, \qquad x_{O2,j} = \frac{(x_{O2,j-1} + k_{O2} I_{j-1})}{(1 + k_{O2} I_{j-1})} \tag{61}$$

and for counter-flow,

$$T_{a,j} = aT_{a,j-1} + (1-a)T_{s,j}, \qquad T_{c,j} = bT_{c,j+1} + (1-b)T_{s,j} \quad (j = 2, \ldots, n+1) \tag{62}$$

$$x_{H2,j} = x_{H2,j-1} + k_{H2} I_{j-1}, \qquad x_{O2,j} = \frac{(x_{O2,j+1} + k_{O2} I_{j-1})}{(1 + k_{O2} I_{j-1})} \tag{63}$$

where

$$a = \frac{1}{(1 + (S_{h,a}\Delta z h_a / c_{a,in} u_{a,in} C_{p,a}))}, \qquad b = \frac{1}{(1 + (S_{h,c}\Delta z h_c / c_{c,in} u_{c,in} C_{p,c}))}, \qquad k_{H2} = \frac{S_{m,a}\xi_{rib}\upsilon_{H2}\Delta z}{n_e F c_{in,a} u_{a,in}}, \qquad k_{O2} = \frac{S_{m,c}\xi_{rib}\upsilon_{O2}\Delta z}{n_e F c_{c,in} u_{c,in}} \tag{64}$$

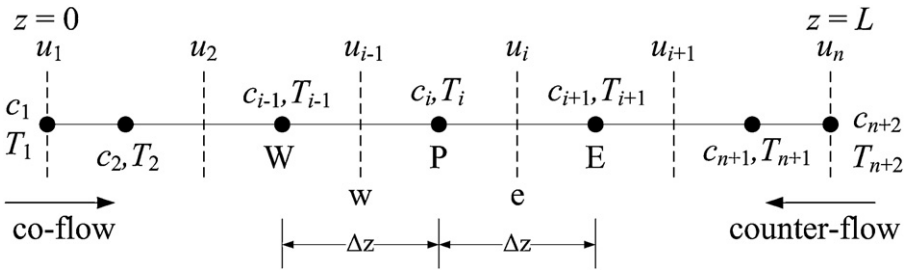

Fig. 7. Discrete scheme of control volumes used in the present work.

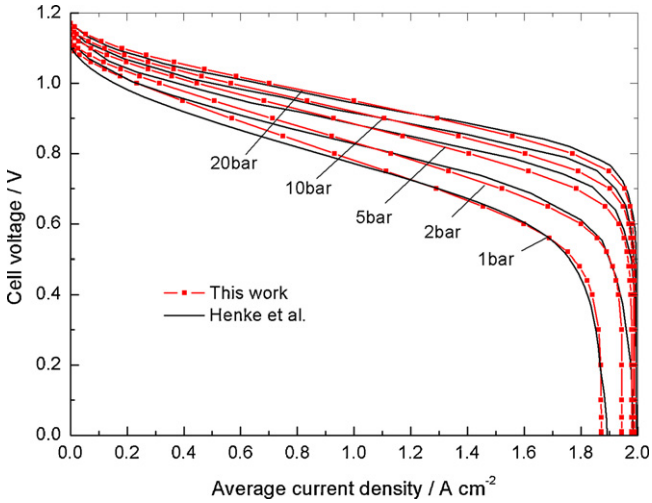

Fig. 8. Comparison between pressure-dependent *V–I* performances of the approximation solution (this work) and numerical elementary kinetic simulation [27]. The parameters are: $l_a = 540\ \mu m$, $l_c = 55\ \mu m$, $l_e = 10\ \mu m$, $W_{ch} = 2\ mm$, $D_{ch,a} = D_{ch,c} = 2\ mm$, $W_{rib} = 2\ mm$, $r_{P,a} = 0.5\ \mu m$, $r_{P,c} = 0.25\ \mu m$, $\varepsilon_a = 0.32$, $\tau_a = 2.9$, $\varepsilon_c = 0.4$, $\tau_c = 1.4$, $\sigma_{ion} = 5.15 \times 10^7/T \exp(-84{,}000/RT)\ S\ m^{-1}$, $\sigma_{el,a} = 9.5 \times 10^7/T \exp(-1150/T)\ S\ m^{-1}$, $\sigma_{el,c} = 4.2 \times 10^7/T \exp(-1200/T)\ S\ m^{-1}$, $E_{act,a} = 130\ kJ\ mol^{-1}$, $E_{act,c} = 125\ kJ\ mol^{-1}$, $\alpha_a = \alpha_c = 0.5$, $i_{0,H2} = 1 \times 10^8\ A\ m^{-3}$, $\nu_{H2} = 0.5$, $\nu_{H2O} = 0$, $T = T_{a,in} = T_{c,in} = T_{ref} = 1073.15\ K$, $I_{eq,fuel} = 2 \times 10^4\ A\ m^{-2}$, $I_{eq,air} = 4 \times 10^4\ A\ m^{-2}$, and the cathode overpotential is calculated by interfacial BV model as $I_{0,O2} = 3.6 \times 10^4\ A\ m^{-2}$, $\nu_{O2} = 0.466$.

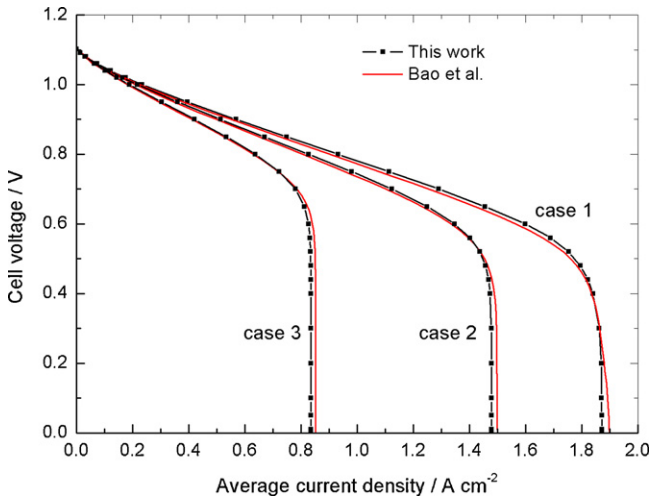

Fig. 9. Comparison between *V–I* performances of the approximate simulation (this work) and a full numerical model [4] under different fuel compositions for case 1: 97% H_2–3% H_2O, case 2: 48.5% H_2–1.5% H_2O–50% N_2, case 3: 19.4% H_2–0.6% H_2O–80% N_2.

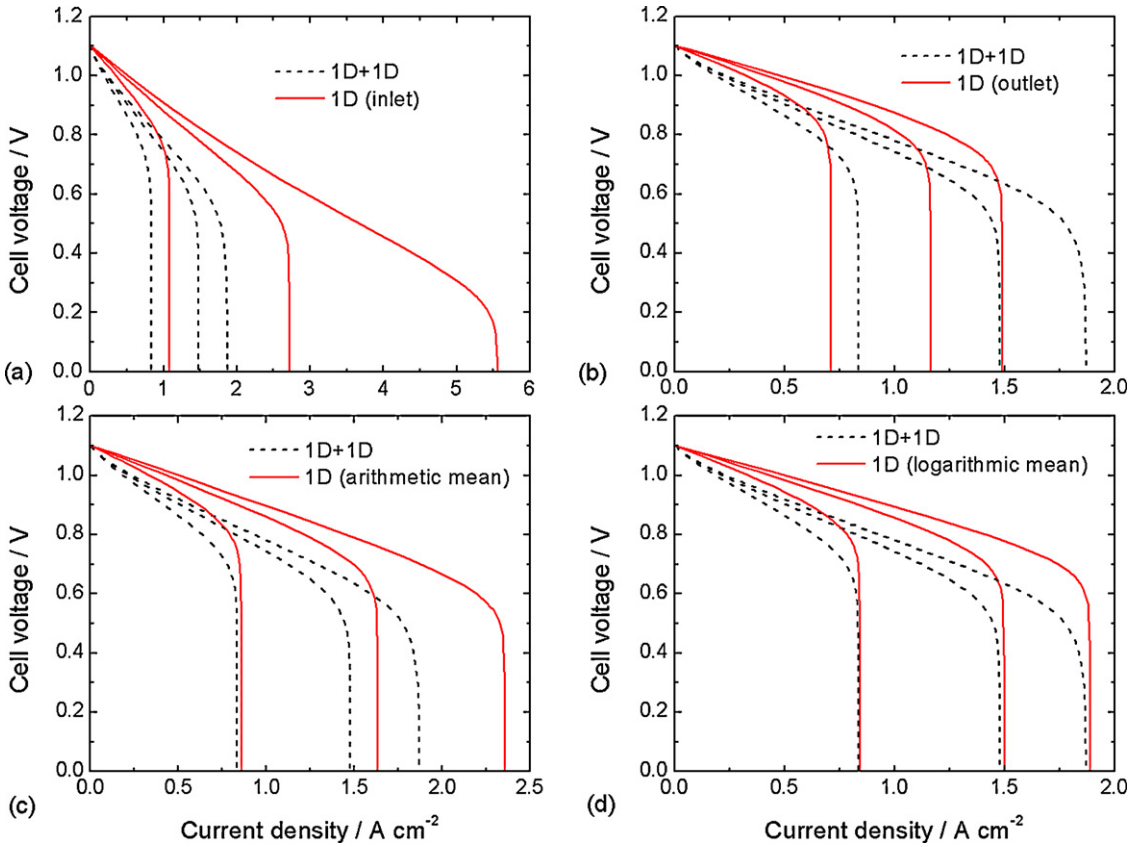

Fig. 10. Comparison between 1D + 1D simulation and 1D simulations (through electrode thickness). The 1D model uses as boundary conditions for bulk concentration at channel/electrode interface (a) 1D + 1D inlet species concentrations, (b) 1D + 1D outlet species concentration, (c) arithmetic mean and (d) logarithmic mean between 1D + 1D inlet and outlet species concentration. Parameters are identical to those in Fig. 8 and the fuel compositions are identical to the three cases in Fig. 9.

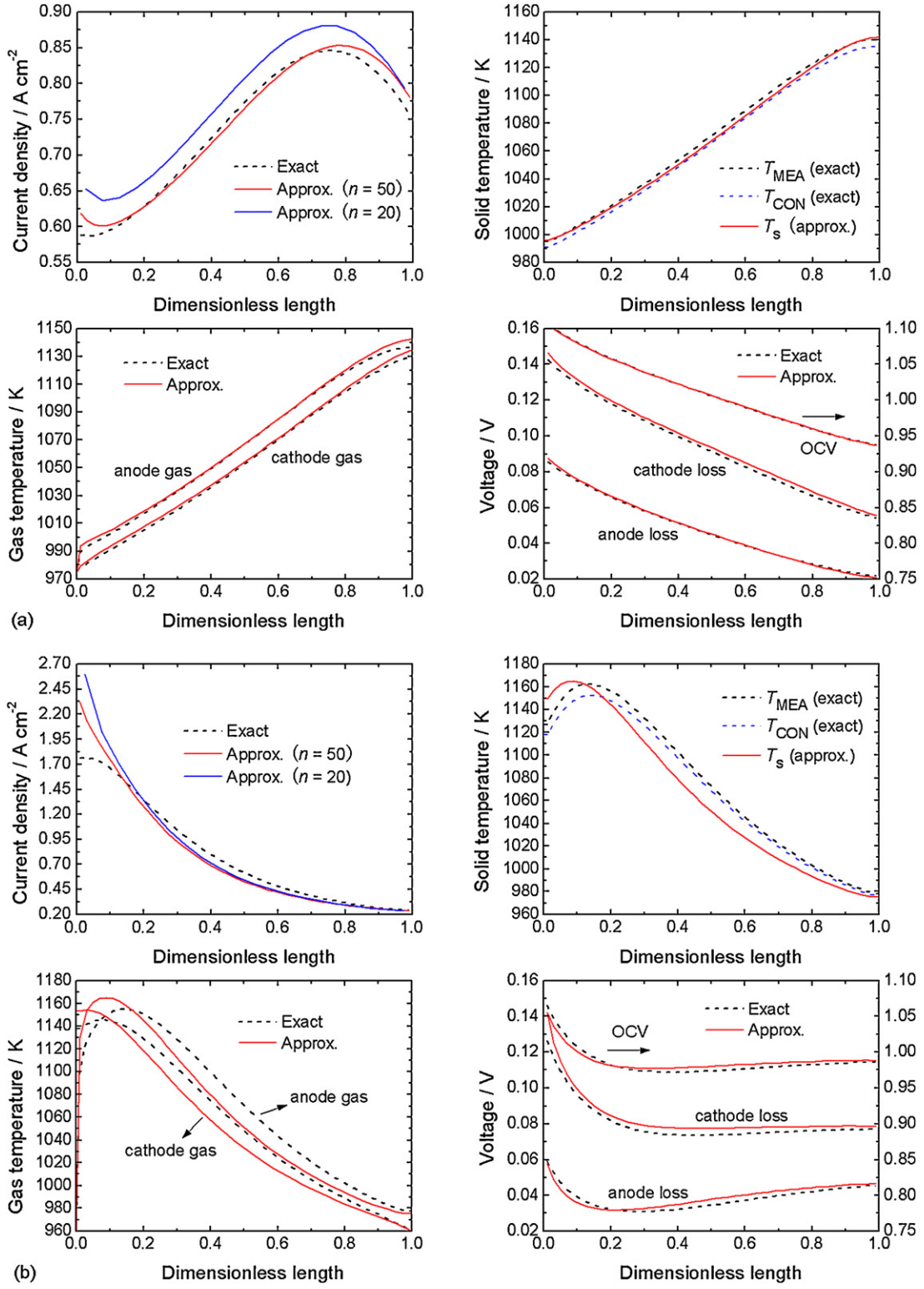

Fig. 11. Along-the-channel profiles of local current density, solid and gas temperatures and overpotentials of both exact and approximate calculations in the case of (a) concurrent flow, (b) countercurrent flow. Fuel composition is 97% H_2–3% H_2O and air is used as oxidant. For concurrent flow, $T_{a,in} = T_{c,in} = 975.15$ K, and for countercurrent flow $T_{a,in} = T_{c,in} = 958.15$ K, other basic parameters are identical to those in Fig. 8.

Substituting Eq. (60) or (62) into Eq. (56), we can get a linear relationship between the local current densities and solid temperatures, $[I] = [A][T_S] + [B]$, which is explained in Appendix B. In this case, the calculating mode with given V_{cell} (cf. Fig. 6) is adopted. Substituting the gas concentrations (Eq. (61) or (63)) as functions of $T_S(z)$ or $I(z)$ into Eqs. (57)–(59), a fast and stable along-the-channel computation can be obtained without V–I iteration loop.

6. Results and discussion

6.1. Isothermal 1D + 1D simulations

We first compare the present model, which is based on a number of approximation assumptions, to two different more complex literature models. Fig. 8 presents the pressure-dependent *V–I* performance of an anode-supported SOFC. Our approximate simulation is compared to a model by Henke et al. [27], which is implemented in an in-house C-code software package DENIS for detailed electrochemistry and numerical impedance simulation. All the cases are isothermal and under countercurrent flow. The inlet fuel and oxidant flow rates are set to a current-density equivalent (I_{eq}) of 2 and 4 A cm^{-2}, respectively. The present model was adjusted to the numerical model by fitting the volumetric exchange current density in the anode, anode average particle size, and H_2 reaction order. The overestimation of the present model in the activation zone is probably due to the different electrochemical kinetics frameworks (one is based on overall Butler–Volmer equation and the other is based on elementary kinetics). On a 2.26 GHz, 1.92 GB PC, the computational time is 0.87 s per point along the IV-curve for the present Matlab-code approximate model (20 along-the-channel control volumes) and average 430 s per point (10 control volumes along the channel length and 22 control volumes along the anode thickness) for the detailed Henke et al. model. These numbers demonstrate the high performance of the present algorithm.

Fig. 9 further compares the *V–I* performance between the approximate simulation and numeric calculation by a model of Bao et al. [4]. The latter is based on a gPROMS implementation of a multi-level SOFC modeling platform [4], which uses the identical physics as described in the present paper, however without approximating assumptions. The comparison is carried out for three different fuel compositions. All the cases are isothermal and under countercurrent flow, and the cell configuration and simulation parameters are identical to those used in Fig. 8. The two simulations are almost identical as predicted both under open circuit conditions as well as under diffusion-limited conditions. The Bao et al. model. [4] (20 along-the-channel control volumes and 15 along-the-anode control volumes based on orthogonal collocation finite elements discretization method) takes average 15 s for each point along *I–V* curve. Therefore, the approximate approach is dozens of times faster than the equation-based solver in gPROMS and furthermore found to be more robust in the activation and concentration loss zone.

6.2. 1D simulations using effective bulk concentrations

As exemplary application of the present model, we compare 1D with 1D + 1D isothermal simulations. For a potential further model reduction, it is interesting to investigate under which boundary conditions a simple 1D model can best represent a more complex 1D + 1D simulation. In particular, we compare four different options for the species bulk concentration at the channel/electrode interface, (i) using the inlet concentration, (ii) using the outlet concentration, (iii) using the arithmetic mean between inlet and outlet concentrations, and (iv) using the logarithmic mean between the inlet and outlet concentrations. Fig. 10 compares the 1D + 1D simulation with these four kinds of 1D simulations under different fuel compositions. As Fig. 10(a) shows, taking the inlet concentration leads to a considerable overestimation of the limiting current density. In this case, consumption of fuel and oxidant cannot be reflected reasonably, which results in the species concentration at the electrode/electrolyte interface even higher than the outlet concentration. According to the upwind scheme in 1D + 1D modeling, the outlet species concentration is taken as the bulk one in each control volume, i.e. each element cell is considered as a continuous stirred-tank reactor (CSTR). However, Fig. 10(b) shows that, using the outlet concentration in 1D simulation results in an obvious underprediction of cell performance. The method of arithmetic mean provides a balance between the first two options, but still leads to an overestimation of the limiting current density as shown in Fig. 10(c). As shown in Fig. 10(d), the logarithmic mean seems to be the best one with regard to the limiting current density. The physical meaning of logarithmic mean concentration can be compared to the logarithmic mean temperature difference in heat exchangers. Bao et al. have previously used the concept of logarithmic mean bulk concentrations in modeling of PEM fuel cells and systems [28,29].

6.3. Full thermal 1D + 1D simulations

Finally, we apply the full thermal 1D + 1D model. Fig. 11 shows along-the-channel profiles of the local current density, solid and gas temperatures and overpotentials. The results of the approximate model (this work) are compared to exact solutions (Bao et al. model [4]) under non-isothermal condition. For these simulations, the inlet fuel and air temperatures were adjusted to values of 702 and 685 °C, which makes the average cell temperature approximately 800 °C. Here, the exact solution in gPROMS [4] considers the radiant heat transfer between the MEA and interconnectors with detailed view factor models, while it is excluded in the approximate calculation due to the assumption of identical local temperature in the both solid phases. As shown in Fig. 11(a) and (b), the approximate model as derived in the present work agrees well with the exact solution under both co-flow and counter-flow conditions. Moreover, the approximation method is found to be rather stable even with a coarse mesh grid. The present model with 20 or 50 along-the-channel control volumes takes only 1.3 and 6.7 s respectively to complete a full thermal 1D + 1D numeration, while it correspondingly takes average 100 or 340 s for the gPROMS-code exact computation.

7. Conclusions

As balance between full mechanistic and semi-empirical fuel cell models, approximate analytical solutions provide a computationally efficient framework with a clear physical meaning. This is an important aspect for multi-scale models and/or real-time simulations of fuel cells, where a compromise needs to be found between computational speed and model precision. In the present work, analytical solutions for 1D through-the-electrode charge and mass transport were developed and integrated into a 1D along-the-channel thermal numerical simulation. The approximation approaches shown in this paper keep the intrinsic nonlinearity of system.

For charge transport and reaction inside a thin porous electrode, overpotential shows a smooth profile and perturbation method generally fails to find a small enough variable. Therefore, a modified Adomian decomposition method (ADM) was applied and validated. Furthermore, an explicit hybrid algorithm of power-law approach and linear approximation based on WKB perturbation method was introduced to overcome some disadvantages in the ADM solution (too many terms, lacking of clear physical meaning, implicit iteration). Although starting from a thick electrode, this algorithm is validated to accurately reflect the boundary-layer effects at both electrode interfaces in a wide range of applications. In addition, a novel expression was developed to interconvert the volume-specific and area-specific exchange current densities, which provides a better theoretical explanation over the common linear relationship via a simple geometric factor.

Exact solutions of mass transfer of different fuel-cell-relevant gas mixtures were then obtained by combining Stephan–Maxwell diffusion equations with the overpotential profiles resulting from the charge transport model. In the case of the H_2–H_2O–CO–CO_2–N_2 system (SOFC anode), by considering H_2/CO co-oxidation, we derived an analytical expression of the ratio of H_2 and CO electrochemical current density. In this regard, the thermodynamic framework can provide a first information for kinetics analysis.

We further integrated the electrode-level model into an along-the-channel simulation. This results in an overall 1D + 1D model, where one dimension is solved analytically and one dimension is solved numerically. For the reactant system of H_2–H_2O–N_2 and O_2–N_2, a linear relationship between the along-the-channel profiles of local current density and solid temperature was further developed in both cases of concurrent and countercurrent flow. The 1D + 1D model was validated by comparison to two different numerical models developed previously by the authors. In addition, when comparing 1D + 1D against 1D models, we found that the logarithmic mean of the inlet and outlet species concentrations can be used as boundary condition at the channel/electrode interface in 1D simulations.

Based on the approximations applied to both dimensions, the computational efficiency of the 1D + 1D model presented in this paper approaches that of a zero-dimensional model. Generally, it only takes several seconds to complete a distributed cell-level simulation, which is valuable for real-time simulations and multi-scale fuel cell models.

Acknowledgements

This work was funded by the Chinese Natural Science Foundation (Project No. 50706019). CB thanks Alexander von Humboldt Foundation for the fellowship for experience researchers. WB acknowledges support from the Initiative and Networking fund of the Helmholtz Association.

Appendix A. WKB perturbation method

Expand the exponent function as Taylor series

$$y'' = k_0[\exp(\alpha_a y) - \exp(-\alpha_c y)] = k_0 \sum_{n=0}^{\infty} \frac{\alpha_a^n - (-\alpha_c)^n}{n!} y^n$$
$$= \lambda^2 \sum_{n=1}^{\infty} a_n y^n \tag{A1}$$

where

$$\lambda = \sqrt{k_0(\alpha_a + \alpha_c)}, \qquad a_n = \frac{\alpha_a^n - (-\alpha_c)^n}{(\alpha_a + \alpha_c)n!} \tag{A2}$$

When k_0 is a large number, $1/\lambda$ can be used as a perturbation variable. Assume

$$y = \exp(\lambda G) \quad \text{and} \quad G = G_0 + \lambda^{-1} G_1 \tag{A3}$$

When only zero-order term of exponent function is considered

$$\sum_{n=1}^{\infty} a_n y^n = \sum_{n=1}^{\infty} a_n e^{\lambda n G} \approx e^{\lambda G} \sum_{n=1}^{\infty} a_n \tag{A4}$$

Substitute Eqs. (A3) and (A4) into Eq. (A1), we obtain

$$G_0'^2 + \lambda^{-1}(2G_0'G_1' + G_0'') = \sum_{n=1}^{\infty} a_n \tag{A5}$$

So,

$$\begin{cases} G_0'^2 = \sum_{n=1}^{\infty} a_n \\ 2G_0'G_1' + G_0'' = 0 \end{cases} \Rightarrow \begin{cases} G_0' = \pm\sqrt{\sum_{n=1}^{\infty} a_n} = \pm\sqrt{\dfrac{e^{\alpha_a} - e^{-\alpha_c}}{\alpha_a + \alpha_c}} \\ G_1 = -\dfrac{1}{2}\ln\ G_0' \end{cases} \tag{A6}$$

Substitute G_0 and G_1 into Eq. (A3), we can obtain the general solution

$$y = c_1\ \exp\left(\lambda\sqrt{\frac{e^{\alpha_a} - e^{-\alpha_c}}{\alpha_a + \alpha_c}}x\right) + c_2\ \exp\left(-\lambda\sqrt{\frac{e^{\alpha_a} - e^{-\alpha_c}}{\alpha_a + \alpha_c}}x\right) \tag{A7}$$

where G_1 has been included in the constant c_1 and c_2.

Appendix B. Linear relationship between current density and solid temperature

From Eqs. (60) and (62), there is

$$\begin{aligned} T_{a,j} - T_{s,j} &= a^{j-1}T_{a,1} + (1-a)\sum_{m=2}^{m=j-1} a^{j-m}T_{s,m} - aT_{s,j} \\ T_{c,j} - T_{s,j} &= b^{j-1}T_{c,1} + (1-b)\sum_{m=2}^{m=j-1} b^{j-m}T_{s,m} - bT_{s,j} \quad \text{(coflow)} \\ T_{c,j} - T_{s,j} &= b^{n-j+2}T_{c,n+2} + (1-b)\textstyle\sum_{m=n+1}^{m=j+1} b^{m-j}T_{s,m} - bT_{s,j} \quad \text{(counterflow)} \end{aligned} \tag{B1}$$

Substitute it into the discrete form of Eq. (56), we obtain the linear relationship between the local current density vector $[I] = [I_1, \ldots I_n]^T$ and the solid temperature vector $[T_s] = [T_{s,2}, \ldots T_{s,n+1}]^T$, i.e. $[I] = [A][T_s] + [B]$, the elements of matrix $[A]$ and $[B]$ are

For concurrent flow

$$\begin{aligned} A_{1,1} &= \frac{-(\gamma_a S_{h,a} h_a a + \gamma_c S_{h,c} h_c b + (\kappa_s/\Delta z^2))}{K} \\ A_{1,2} &= \frac{\kappa_s}{K\Delta z^2}, \quad A_{1,j} = 0 \quad (j = 3 \ldots n) \\ A_{i,j} &= \frac{[\gamma_a S_{h,a} h_a (1-a) a^{i-j+2} + \gamma_c S_{h,c} h_c (1-b) b^{i-j+2}]}{K} \quad (j = 1 \ldots i-2) \\ A_{i,i-1} &= \frac{[\gamma_a S_{h,a} h_a (1-a) a + \gamma_c S_{h,c} h_c (1-b) b + (\kappa_s/\Delta z^2)]}{K} \\ A_{i,i} &= \frac{-(\gamma_a S_{h,a} h_a a + \gamma_c S_{h,c} h_c b + (2\kappa_s/\Delta z^2))}{K} \\ A_{i,i+1} &= \frac{\kappa_s}{K\Delta z^2} \quad (i = 2 \ldots n-1) \\ A_{n,j} &= \frac{[\gamma_a S_{h,a} h_a (1-a) a^{n-j+2} + \gamma_c S_{h,c} h_c (1-b) b^{n-j+2}]}{K} \quad (j = 1 \ldots n-2) \\ A_{n,n-1} &= \frac{[\gamma_a S_{h,a} h_a (1-a) a + \gamma_c S_{h,c} h_c (1-b) b + (\kappa_s/\Delta z^2)]}{K} \\ A_{n,n} &= \frac{-(\gamma_a S_{h,a} h_a a + \gamma_c S_{h,c} h_c b + (\kappa_s/\Delta z^2))}{K} \end{aligned} \tag{B2}$$

$$B_i = \frac{(\gamma_a S_{h,a} h_a a^i T_{a,in} + \gamma_c S_{h,c} h_c b^i T_{c,in})}{K} \quad (i = 1 \ldots n) \tag{B3}$$

For countercurrent flow

$$A_{1,1} = \frac{-(\gamma_a S_{h,a} h_a a + \gamma_c S_{h,c} h_c b + (\kappa_s/\Delta z^2))}{K}$$
$$A_{1,2} = \frac{[\gamma_c S_{h,c} h_c (1-b) b + (\kappa_s/\Delta z^2)]}{K}$$
$$A_{1,j} = \frac{\gamma_c S_{h,c} h_c (1-b) b^{j-1}}{K} \quad (j = 3 \ldots n)$$
$$A_{i,j} = \frac{\gamma_a S_{h,a} h_a (1-a) a^{i-j+2}}{K} \quad (j = 1 \ldots i-2)$$
$$A_{i,i-1} = \frac{[\gamma_a S_{h,a} h_a (1-a) a + (\kappa_s/\Delta z^2)]}{K} \quad (i = 2 \ldots n-1)$$
$$A_{i,i} = \frac{-(\gamma_a S_{h,a} h_a a + \gamma_c S_{h,c} h_c b + (2\kappa_s/\Delta z^2))}{K} \tag{B4}$$
$$A_{i,i+1} = \frac{[\gamma_c S_{h,c} h_c (1-b) b + (\kappa_s/\Delta z^2)]}{K}$$
$$A_{i,j} = \frac{\gamma_c S_{h,c} h_c (1-b) b^{j-i}}{K} \quad (j = i+2 \ldots n)$$
$$A_{n,j} = \frac{\gamma_a S_{h,a} h_a (1-a) a^{n-j}}{K} \quad (j = 1 \ldots n-2)$$
$$A_{n,n-1} = \frac{[\gamma_a S_{h,a} h_a (1-a) a + \gamma_c S_{h,c} h_c (1-b) b + (\kappa_s/\Delta z^2)]}{K}$$
$$A_{n,n} = \frac{-(\gamma_a S_{h,a} h_a a + \gamma_c S_{h,c} h_c b + (\kappa_s/\Delta z^2))}{K}$$

$$B_i = \frac{(\gamma_a S_{h,a} h_a a^i T_{a,in} + \gamma_c S_{h,c} h_c b^{n-i+1} T_{c,in})}{K} \quad (i = 1 \ldots n) \tag{B5}$$

where the adiabatic conditions of solid phase, $\partial T_s/\partial z\big|_{z=0} = \partial T_s/\partial z\big|_{z=L} = 0$ have been included and the denominator K is

$$K = \xi_{rib} \gamma_c S_{m,c} \left(V_{cell} + \frac{\Delta H_{ref}}{n_e F} \right) \tag{B6}$$

References

[1] M.P. Eschenbach, R. Coulon, A.A. Franco, J. Kallo, W.G. Bessler, Solid State Ionics 192 (2011) 615–618.
[2] W.G. Bessler, S. Gewies, M. Vogler, Electrochimica Acta 53 (2007) 1782–1800.
[3] W.G. Bessler, ECS Transactions 35 (2011) 859–869.
[4] C. Bao, Y.X. Shi, E. Croiset, C. Li, N.S. Cai, Journal of Power Sources 195 (2010) 4871–4892.
[5] C. Bao, Y.X. Shi, C. Li, N.S. Cai, Q.Q. Su, International Journal of Hydrogen Energy 35 (2010) 2894–2899.
[6] A. Bieberle, L.J. Gauckler, Solid State Ionics 146 (2002) 23–41.
[7] W.G. Bessler, Solid State Ionics 176 (2005) 997–1011.
[8] T.E. Springer, T. Rockward, T.A. Zawodzinski, S. Gottesfeld, Journal of the Electrochemical Society 148 (2001) A11–A23.
[9] H. Yakabe, T. Ogiwara, M. Hishinuma, I. Yasuda, Journal of Power Sources 102 (2001) 144–154.
[10] T. Ackmann, L.G.J. de Harrt, W. Lehnert, D. Stolten, Journal of the Electrochemical Society 150 (2003) A783–A789.
[11] S. Mazumder, J.V. Cole, Journal of the Electrochemical Society 150 (2003) A1503–A1517.
[12] J.W. Kim, A.V. Virkar, K.Z. Fung, K. Mehta, S.C. Singhal, Journal of the Electrochemical Society 146 (1999) 69–78.
[13] R.F. Mann, J.C. Amphlett, M.A.I. Hooper, H.M. Jensen, B.A. Peppley, P.R. Roberge, Journal of Power Sources 86 (2000) 173–180.
[14] V. Gurau, F. Barbir, H. Liu, Journal of the Electrochemical Society 147 (2000) 2468–2477.
[15] C.R. Tsai, F. Chen, A.C. Ruo, M.H. Chang, H.S. Chu, C.Y. Soong, W.M. Yan, C.H. Cheng, Journal of Power Sources 160 (2006) 50–56.
[16] P. Costamagna, P. Costa, V. Antonucci, Electrochimica Acta 43 (1998) 375–394.
[17] C. Bao, N.S. Cai, AIChE Journal 53 (2007) 2968–2979.
[18] Y. Sung, Journal of Power Sources 159 (2006) 1051–1060.
[19] F.A. Coutelieris, S.L. Douvartzides, P.E. Tsiakaras, Chemical Engineering Science 60 (2005) 4423–4430.
[20] A.A. Kulikovsky, Analytical Modelling of Fuel Cells, Elsevier, Amsterdam, 2010.
[21] G. Adomian, Solving Frontier Problems of Physics: The Decomposition Method, Kluwer, Boston, MA, 1994.
[22] A.M. Wazwaz, S.M. El-Sayed, Applied Mathematics and Computation 122 (2001) 393–405.
[23] A.H. Nayfeh, Introduction to Perturbation Techniques, John Wiley & Sons, New York, 1981.
[24] A. Bertei, A.S. Thorel, W.G. Bessler, C. Nicolella, Chemical Engineering Science 68 (2012) 606–616.
[25] P. Heidebrecht, K. Sundmacher, Fuel Cells 2 (2002) 166–180.
[26] S.V. Patankar, Numerical Heat Transfer and Fluid Flow, McGraw-Hill, New York, 1980.
[27] M. Henke, J. Kallo, K.A. Friedrich, W.G. Bessler, Fuel Cells 4 (2011) 581–591.
[28] C. Bao, M.G. Ouyang, B.L. Yi, Journal of Power Sources 156 (2006) 232–243.
[29] C. Bao, M.G. Ouyang, B.L. Yi, International Journal of Hydrogen Energy 31 (2006) 1040–1057.